

Additive Manufacturing of 3D Luminescent $\text{ZrO}_2\text{:Eu}^{3+}$ Architectures

Jędrzej Winczewski,* Manuel Herrera, Clément Cabriel, Ignacio Izeddin, Stefan Gabel, Benoit Merle, Arturo Susarrey Arce,* and Han Gardeniers*

Implementation of more refined structures at the nano to microscale is expected to advance applications in optics and photonics. This work presents the additive manufacturing of 3D luminescent microarchitectures emitting light in the visible range. A tailor-made organo-metallic resin suitable for two-photon lithography is developed, which upon thermal treatment in an oxygen-rich atmosphere allows the creation of silicon-free tetragonal (*t*-) and monoclinic (*m*-) ZrO_2 . The approach is unique because the tailor-made Zr-resin is different from what is achieved in other reported approaches based on sol-gel resins. The Zr-resin is compatible with the Eu-rich dopant, a luminescent activator, which enables to tune the optical properties of the ZrO_2 structures upon annealing. The emission characteristics of the Eu-doped ZrO_2 microstructures are investigated in detail with cathodoluminescence and compared with the intrinsic optical properties of the ZrO_2 . The hosted Eu has an orange-red emission showcased using fluorescence microscopy. The presented structuring technology provides a new platform for the future development of 3D luminescent devices.

with emissions ranging from ultraviolet to near-infrared.^[7–9] Such radiation has a long-lived 4f–4f transition, observed when evaluating lanthanides resulting in sharp narrowband emission. This light emission can be supported even when incorporating the lanthanide ion in a dispersion medium that acts as a host matrix with diverse functionalities.^[7,9]

Two host matrix types for lanthanide ions are identified, namely, organic^[10] and inorganic materials.^[7,11] Inorganic materials have high lattice-binding energy combined with rigidity; thus, in most cases, they show greater chemical and thermal resistance and photostability against continuous excitation than organic materials.^[1,8] Highly crystalline inorganic host matrices are typically preferred to reduce point defects emissions. Hence, attention should be given to the crystallinity of the host material and the nonradiative

phonon relaxation caused by the crystal lattice.^[9] In practice, low phonon energy hosts are preferred to utilize the luminescent activator effectively.^[7] However, the commonly used SiO_2 ($\approx 1100\text{ cm}^{-1}$ stretching vibration) presents low lanthanide solubility,^[12,13] leading to cluster formation at high dopant contents (10^{18} cm^{-3}),^[14] quenching the lanthanide emission.^[13] In photonics, a substitute for SiO_2 is ZrO_2 , which has relatively good transparency in the visible and infrared range and low phonon energy ($\approx 470\text{ cm}^{-1}$).^[12] ZrO_2 occurs in three polymorphs, tetragonal, monoclinic, and cubic, denoted *t*- ZrO_2 , *m*- ZrO_2 , and

1. Introduction

Materials doped with luminescent lanthanides have found applications in lasers, displays, lighting, and optical fibers,^[1] with advanced applications in the field of bioimaging,^[2] light-emitting diodes,^[3] luminescence thermometry,^[4] theragnostic,^[5] microlasers,^[6] and waveguides.^[7] Such a variety of applications is due to the lanthanide optical properties that stem from their $[\text{Xe}]4f^N$ ($N = 0\text{--}14$) electronic configurations.^[7,8] The underlying ladder-like energy levels enable radiative transitions

J. Winczewski, A. Susarrey Arce, H. Gardeniers
Mesoscale Chemical Systems
MESA+ Institute
University of Twente
P.O. Box 217, Enschede 7500 AE, The Netherlands
E-mail: j.p.winczewski@utwente.nl; a.susarreyarce@utwente.nl;
j.g.e.gardeniers@utwente.nl

 The ORCID identification number(s) for the author(s) of this article can be found under <https://doi.org/10.1002/adom.202102758>.

© 2022 The Authors. Advanced Optical Materials published by Wiley-VCH GmbH. This is an open access article under the terms of the Creative Commons Attribution License, which permits use, distribution and reproduction in any medium, provided the original work is properly cited.

DOI: 10.1002/adom.202102758

M. Herrera
Centro de Nanociencias y Nanotecnología
Universidad Nacional Autónoma de México
Km 107 Carretera Tijuana-Ensenada, Ensenada
Baja California C.P. 22800, Mexico
C. Cabriel, I. Izeddin
Institut Langevin
ESPCI Paris
CNRS
PSL University
1 rue Jussieu, Paris 75005, France
S. Gabel, B. Merle
Materials Science & Engineering, Institute I
Interdisciplinary Center for Nanostructured Films (IZNF)
Friedrich-Alexander-Universität Erlangen-Nürnberg (FAU)
Cauerstr. 3, D-91058 Erlangen, Germany

c -ZrO₂, all broadly applied as a host of trivalent phosphors such as Dy³⁺, Eu³⁺, Gd³⁺, Tb³⁺, and Tm³⁺.^[15,16] Among these examples, Eu³⁺ exhibits a sharp emission band corresponding to red and orange-red in the color space chromaticity diagram.^[17] The characteristics and dynamics of the Eu³⁺ radiative transitions display high sensitivity to the local environment of the ZrO₂ lattice.^[18] For *t*-ZrO₂-hosted Eu³⁺, two emission lines of similar intensities are typically observed, one at ≈590 nm (⁵D₀ → ⁷F₁, from unresolved two allowed transitions) and a second at ≈606 nm (⁵D₀ → ⁷F₂).^[18] Furthermore, depending on the crystal structure, local symmetry results in an emission characteristic, dominated by ⁵D₀ → ⁷F₂ transition within the 611–618 nm range, with one or weaker lines between 577 and 580 nm (⁵D₀ → ⁷F₀) as known for *m*-ZrO₂.^[18] In case of *c*-ZrO₂, four lines at 575 nm (⁵D₀ → ⁷F₀), 590 nm (⁵D₀ → ⁷F₁), 607 nm (⁵D₀ → ⁷F₂), and 636 nm (⁵D₀ → ⁷F₃) are observed.^[19,20] From these examples, it is clear that emission characteristics of Eu³⁺ can be tuned as a function of the ZrO₂ crystal structure.

Several chemical methods have produced crystalline ZrO₂-hosted Eu³⁺ (ZrO₂:Eu³⁺). These include coprecipitation,^[21] hydrothermal,^[22] solvothermal,^[23] and sol-gel method,^[24] leading to nanoparticle formation.^[25] Selected examples of ZrO₂:Eu³⁺ of morphologies different than particles include thin films,^[26] inverse opals,^[27] nanotube arrays,^[25] xerogels,^[28] and nanofibers.^[29] However, a production process of 3D-architected ZrO₂:Eu³⁺ that combines micro(nano)structural features which can be readily integrated into standard cleanroom process flows has not yet been reported.

A way forward is additive manufacturing (AM). AM has the advantage of high processability and can produce 3D luminescent architectures.^[30,31] Among the AM processes allowing genuinely 3D fabrication of complex structures, two-photon lithography (TPL) has emerged as a state-of-the-art method that permits structural shaping with sub-micrometer precision bridging the gaps between the micro and nanoscale.^[32–34] In TPL, the focused femtosecond laser radiation is applied to generate radicals or cations locally, initiating two-photon polymerization of negative-tone photoresists, which solidify in desired areas only.^[34,35] Micro- and nano-objects of virtually any arbitrary geometry can be manufactured by rastering the position of the focal spot within the photoresist in 3D.^[34]

In practice, TPL is primarily utilized to fabricate structures from commercially available organic resins, limiting the application scope.^[34] New material combinations must be explored to unleash the full potential of TPL and enable the 3D printing of metals, metal oxides, and ceramics to foster the manufacturing of multifunctional materials.^[36] Thus far, two main strategies have been implemented for manufacturing such 3D materials using TPL: i) the *ex situ* approach based on the functionalization of polymeric structures after their photopolymerization, and ii) direct printing using tailor-made resins.^[37–39]

For the (i) *ex situ* approach, the 3D-printed lattices act as templates. The lattice is conformally coated with a metal, metal oxide, or ceramic material to obtain composite core–shell structures. Methods like atomic layer deposition (ALD),^[40,41] electro-deposition,^[42] or electroless plating^[43,44] are typically used to coat such 3D printed architectures. Examples of the deposited layers include Al₂O₃,^[45] TiN,^[38] ZnO,^[41] TiO₂,^[41,46] CoNi,^[42] or Ag.^[44] Upon removal of the organic constituents of the sacrificial

lattice, e.g., with oxygen plasma, through a small opening, hollow-beam structures (e.g., Al₂O₃) can be achieved.^[38,47]

For route (ii), direct printing with a tailor-made resin approach, either nanofilled or organic–inorganic resin, is used. For nanofilled resins, nanoparticles (NPs) are dispersed in a compatible monomeric matrix via stirring. Usually, the resins are filled with metal or metal oxide nanoparticles to modify the electric, magnetic, or optical properties.^[37,48,49] One of the identified limitations of the nanofiller-based approach is that the photolithography process is affected by the NPs properties. Illumination of the NPs dispersed in resins can provoke light scattering affecting the final 3D-printed architecture.^[50,51] Furthermore, as the structure dimensions increase (going from voxel clusters to longer beams), high nanofiller loadings may be required, leading to the promotion of light scattering and compromising the lateral resolution during printing.^[52] These two disadvantages, in practice, render the nanofiller resins unsuitable for the fabrication of complex 3D architectures of fine feature sizes.^[53] Organic–inorganic resins free of nanofillers have been extensively investigated and developed to circumvent these limitations.^[39,54,55]

Preparing a custom-made photosensitive organic-inorganic resin is laborious since a one-pot synthesis process is not trivial.^[39] Typically, organic–inorganic resins incorporate different polymerizable condensation products between the adequate metal- or metalloid-alkoxides and (meth)acrylic acid. The composition of the material obtained after thermal treatment is very much dependent on the polymerized monomeric species. Including metals or metalloids in the organic–inorganic resin matrix and controlling the atmosphere during annealing provides sufficient versatility for producing 3D-printed structures of the desired composition.^[56] For example, pyrolysis of crosslinked acrylate siloxanes in N₂ yields SiC,^[57] whereas annealing in air results in the formation of SiOC.^[58] Other compositions have been reported using hybrid sol-gel resins containing more than one metal or a metalloid, such as an acrylate siloxane complex with zirconium^[59] or germanium.^[60] Besides the monomers based on the silicon-oxygen backbone, the availability of resins fostering fabrication of certain dopant-free metal-oxides (e.g., SnO₂,^[61] TiO₂,^[52,62] ZnO^[55]) may turn out to be advantageous for tuning the electronic and optical properties of the self-miniaturized polycrystalline 3D-printed structure.^[63]

To date, the fabrication of sub-micrometer silicon-free zirconia using organic–inorganic resins via TPL has not been achieved.^[64] Although Buchegger et al. reported the fabrication of polymeric woodpile architectures by stimulated emission depletion lithography, the applied resin contained up to 5% of the methacrylate-substituted zirconium oxo cluster [Zr₄O₂(OMc)₁₂]. The study was dedicated to partially replacing the methacrylate ligands in Zr₄O₂(OMc)₁₂ to foster the later thiol-driven functionalization of the resultant inorganic–organic polymer.^[65] It should be noted that the printed structures were not annealed, and the highest Zr₄O₂(OMc)₁₂ applied loading corresponds to ≈1.3 wt% of Zr. Structures printed from the commercially available SZ2080 resin, which contains both Si and Zr, could thus far be transformed into inorganic glass-ceramic composed of cristobalite and tetragonal zirconia.^[59,60] In retrospect, silicon-free zirconia can be the next steppingstone to manufacture well-dispersed red-emitting 3D-printed ZrO₂ structures.

This work presents the fabrication of silicon-free 3D zirconia microstructures using a custom-made organo-metallic acrylic resin compatible with the two-photon lithography process. The additively manufactured 3D metal-organic polymeric networks are annealed in atmospheric air in a chamber oven, which removes organic components and forms ZrO_2 replicas. The annealing of the printed structures in the air at 600 °C results in the formation of *t*- ZrO_2 . In the following step, *t*- ZrO_2 is gradually transformed with a temperature ramp-up to yield *m*- ZrO_2 at 1050–1200 °C. The functionality of our ZrO_2 -photoresist is assessed with the incorporation of Eu^{3+} , enabling tuning not only the chemical composition of obtained ZrO_2 3D structures but also their optical properties. The addition of 3 mol% of Eu^{3+} -containing salt to the resin eases the formation of $ZrO_2:Eu^{3+}$. Optical properties of the $ZrO_2:Eu^{3+}$ printed structures are investigated using cathodoluminescence (CL). For the undoped *t*- ZrO_2 , multiple emission bands within 1.65–3.5 eV and *m*- ZrO_2 in the 2.3–2.9 eV range are detected. The fabricated *m*- $ZrO_2:Eu^{3+}$ and *t*- $ZrO_2:Eu^{3+}$ structures exhibit characteristic intense $^5D_0-^7F_1$ and $^5D_0-^7F_2$ transitions. The orange-red emission from the *m*- $ZrO_2:Eu^{3+}$ 3D architecture is showcased using wide-field fluorescence microscopy. Our approach promotes the creation of ZrO_2 of tunable chemical composition via a one-pot resin preparation process. From a broad perspective, our AM approach can expand the ongoing trend of dimensionally refined functional luminescent materials, uniting materials science with optoelectronics.

2. Results and Discussion

A resin allowing the AM of Si-free Eu-doped ZrO_2 microstructures of sub-micrometer feature sizes has been developed. First, the control of the crystallographic phase of polymer-derived

ZrO_2 microstructures is presented. Next, the resin doping with Eu is highlighted, enabling the fabrication of $ZrO_2:Eu^{3+}$ luminescent microstructures.

2.1. Additive Manufacturing of *t*- ZrO_2 and *m*- ZrO_2 Microarchitectures

Zirconia 3D architectures are fabricated using a custom organic-inorganic resin suitable with two-photon lithography. First, zirconium acrylate (ZrA) is dissolved in *N,N*-dimethylacetamide (DMAc), and dichloromethane (DCM) in the presence of acrylic acid (AA). Then, a multifunctional crosslinking agent, pentaerythritol triacrylate (PETA), and a two-photon photoinitiator, 7-Diethylamino-3-thenoylcoumarin (DETC), are added to the mixture (Figure 1a). DCM is used to accelerate the dissolution of zirconium acrylate and is removed under reduced pressure upon the dissolution of ZrA and DETC. The resulting orange-yellow solution contains $\approx 0.2 \times 10^{-3}$ M of Zr and 2.2 wt% of the photoinitiator. The DMAc is selected due to the low vapor pressure and the polar character allowing the dissolution of various inorganic and organometallic salt additives.^[66,67]

The prepared organic-inorganic resin is drop-casted onto a glass slide and covered with an 8 × 8 mm silicon wafer dice placed on two polyimide spacers (Figure 1b). Such a configuration allows retaining resin within the working distance of the commercial two-photon lithography system (Photonic Professional GT, Nanoscribe). The various 3D microarchitectures (gyroid, octet-truss lattice, supported buckyball) are printed directly on silicon substrates using TPL (Figure 1b) and later developed in dimethyl sulfoxide (DMSO) and isopropanol (IPA) for removal of the non-cured resin. Subsequently, the structures are annealed in atmospheric air in a chamber oven at 600, 750, 900, 1050, and 1200 °C for 1 h (Figure 1d).

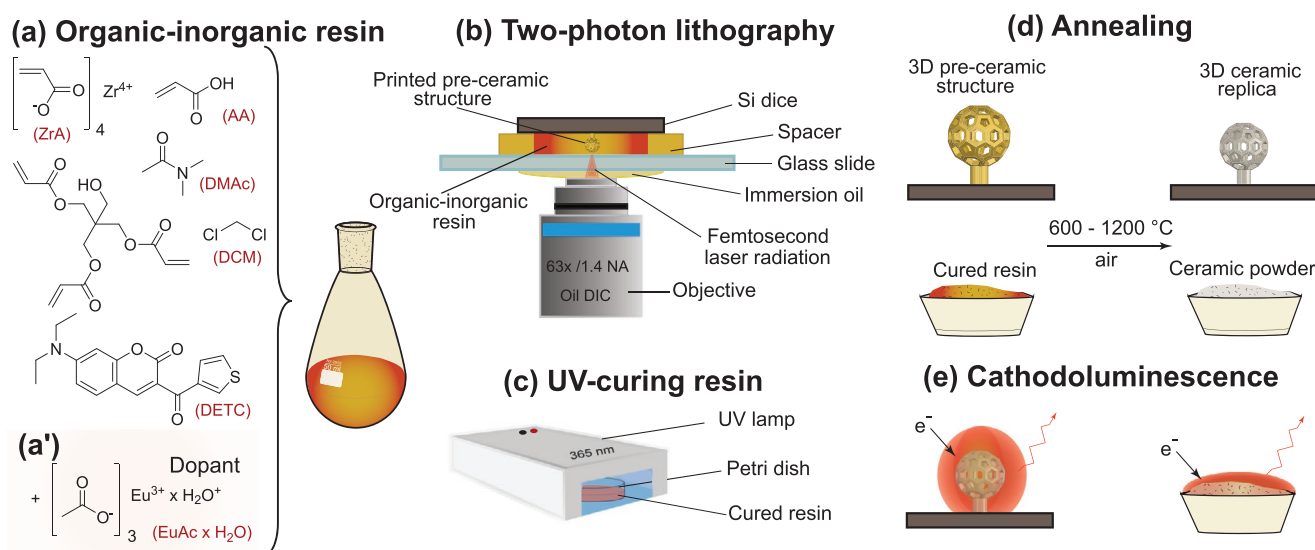


Figure 1. Fabrication route of 3D zirconia and europium-doped zirconia microstructures using two-photon lithography. a) Preparation of organic-inorganic resin by dissolving ZrA, DETC, and PETA in AA, DMAc, and DCM. a') $EuOAc \times H_2O$ is added as a resin dopant for the Eu-containing resin. b) Additive manufacturing 3D pre-ceramic structures (ZrO_2 or $ZrO_2:Eu^{3+}$) on a silicon substrate via TPL using the custom organic-inorganic resin. c) UV-curing of the custom resins. d) Annealing of the 3D pre-ceramic structures and cured resins at 600–1200 °C for 1 h, resulting in isotropically shrunken ZrO_2 replicas, or powder, respectively. e) Cathodoluminescence of the $ZrO_2:Eu^{3+}$ 3D structures and the $ZrO_2:Eu^{3+}$ ceramic powder.

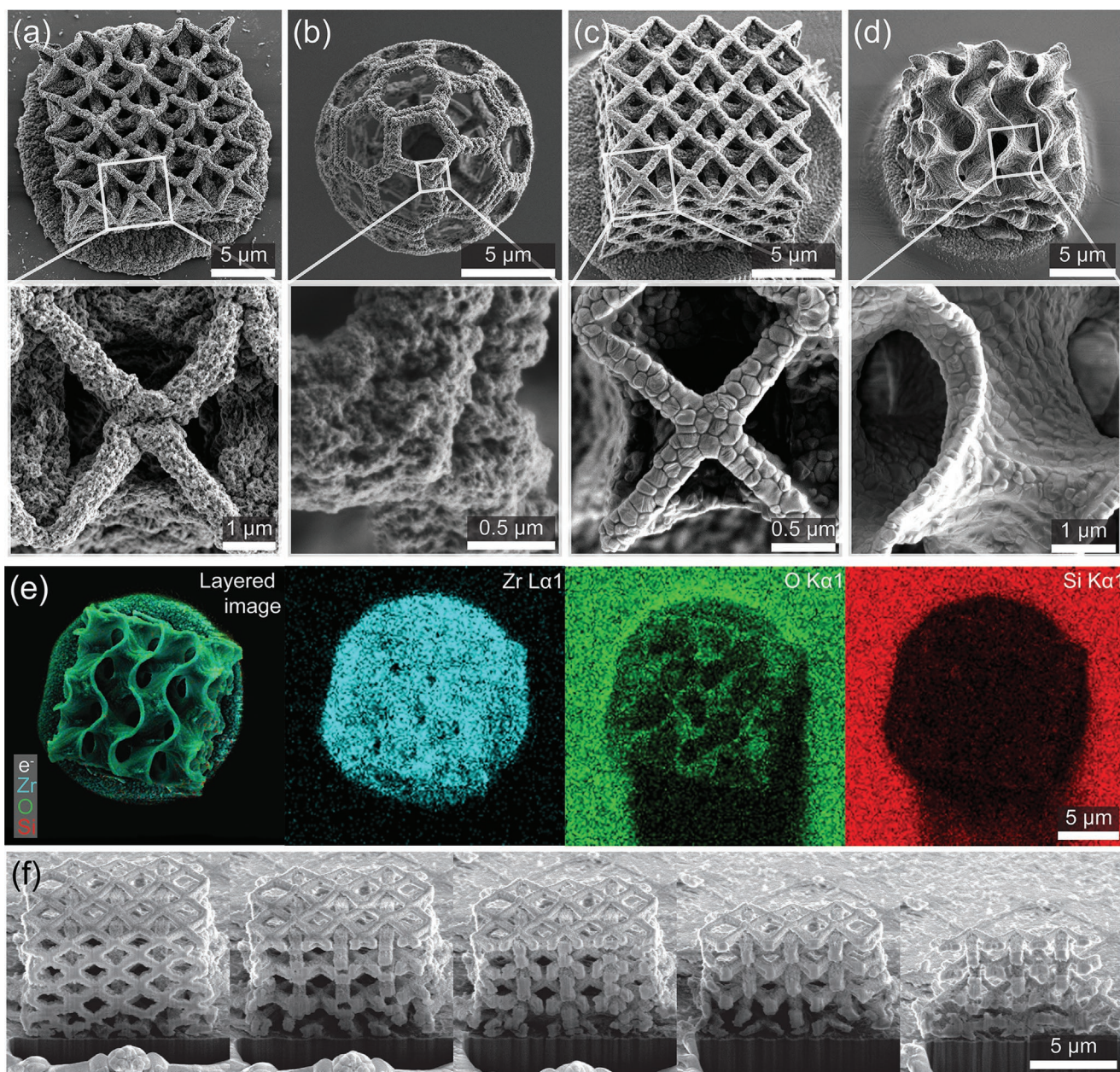


Figure 2. Characterization of the 3D-printed ZrO₂ structures. Scanning electron microscopy (SEM) images of ZrO₂: a) Octet-truss lattice annealed at 600 °C for 1 h; b) buckyball annealed at 900 °C; c) octet-truss lattice annealed at 1200 °C; d) gyroid annealed at 1200 °C; the close-up high-magnification SEM images represent the areas marked with the rectangular boxes. e) SEM-EDS maps showing the distribution of Zr, O, and Si (substrate) over a gyroid annealed at 1200 °C for 1 h. f) FIB tomography of an octet-truss lattice annealed at 600 °C for 1 h. Scale bars (a–f) represent 5 μm; in the close-up (a–d) images the scale bars are (a, d) 1 μm, (b, c) 500 nm.

The process is associated with $\approx 60\%$ isotropic linear shrinkage and yields self-miniaturized solid ZrO₂ replicas. Scanning electron microscopy (SEM) images of 3D-printed annealed structures are shown below (Figure 2a–d). A representative SEM image of the pre-ceramic gyroid is presented in Figure S1a (Supporting Information). The annealing at 600 °C results in the formation of finely grained *t*-ZrO₂, presented for an octet-truss lattice in Figure 2a. The annealing at 900 °C results in partly transformed ZrO₂, associated with the growth of the grains, depicted for a buckyball (Figure 2b), octet truss

lattice (Figure 2c), and gyroid (Figure 2d) structures. The octet truss lattice thermally processed at 1200 °C consists of crystallites of 224.3 ± 65.4 nm average diameter (Figure S2a–c, Supporting Information). The spatial chemical composition of the fabricated annealed structures determined with energy-dispersive X-ray spectroscopy (EDS) is presented in Figure 2e. Both O and Zr are uniformly distributed throughout the architecture. Si is only present in the substrate and absent in the printed structure. Individual Si-indexed pixels are present in the areas matching the cavities and support layer in the gyroid structure,

attainable for the typical reactive volumes for characteristic X-rays in EDS analysis.^[68] The annealing of Si substrates on which structures are printed results in surface oxide layer formation, as confirmed in the SEM-EDS maps showing Si and O distribution (EDS (Figure 2e)). The thickness of SiO₂ depends on the temperature, duration of the annealing, and atmosphere, and may reach hundreds of nanometers.^[69] SiO₂ growth is not identified to be detrimental to the adhesion of the printed 3D structures under the range of conditions applied during the annealing step. The structural integrity of a manufactured 3D octet-truss ZrO₂ lattice annealed at 600 °C is inspected with focused ion beam (FIB) tomography (Figure 2f). The beams are solid throughout the architecture, indicating adequate 3D design slicing parameters for a TPL process. The periodic lattice morphology is preserved, and no discernible regions with broken or discontinuous features can be found, as confirmed in Video S1 (Supporting Information).

The phases of ZrO₂ are known to possess different crystallographic and optical properties. From this viewpoint, accurate control of the 3D structure crystallinity is crucial for realizing specific functionalities. The influence of annealing conditions on the crystallinity of the polymer-derived ZrO₂ replicas of 3D-printed structures is analyzed using confocal Raman spectroscopy at 532 nm excitation wavelength (Figure 3a, labeled in red). Samples annealed at 600, 750, 900, 1050, and 1200 °C are characterized. The spectrum acquired for the sample annealed at 600 °C shows vibrational modes at 146 cm⁻¹ (B_{1g}), 267 cm⁻¹ (E_g), 314 cm⁻¹ (B_{1g}) and two broad bands at 460 cm⁻¹ (E_g), and 642 cm⁻¹ (E_g), assigned to the *t*-ZrO₂ phase.^[70–72] For the sample annealed at 750 °C, two additional shoulders at 476 and 596 cm⁻¹ are observed, which may indicate the appearance of trace amounts of *m*-ZrO₂.^[71–73] The spectrum registered for structures annealed at 900 °C is dominated by *t*-ZrO₂ content. The observed bands are likely broadened due to the superposition with *m*-ZrO₂ signals. Upon deconvolution (Figure S3, Supporting Information), vibrational modes of *t*-ZrO₂ at 148 cm⁻¹

(B_{1g}), 268 cm⁻¹ (E_g), 464 cm⁻¹ (E_g), 606 cm⁻¹ (B_{1g}), and 649 cm⁻¹ (E_g) are recognized. The contributions at 321 cm⁻¹ (A_g) and 524 cm⁻¹ (B_g) can likely be assigned to *m*-ZrO₂.^[70–72] The contributions of *m*-ZrO₂ are of minor intensity, and their location is strongly superposed with other narrowly distributed vibrational modes of ZrO₂. Due to the open lattice character of the structures, a background peak at 521 cm⁻¹ originating from the crystalline Si substrate (Figure S4, Supporting Information) may be observed during signal acquisition, which may partially overlap with B_g *m*-ZrO₂.^[74] Spectra registered for samples calcined at 1050 and 1200 °C are characterized by the presence of typical *m*-ZrO₂ vibrational modes at 172 cm⁻¹ (B_g), 185 cm⁻¹ (A_g), 215 cm⁻¹ (B_g), 298 cm⁻¹ (B_g), 302 cm⁻¹ (B_g), 328 cm⁻¹ (B_g), 340 cm⁻¹ (A_g), 377 cm⁻¹ (A_g + B_g), 471 cm⁻¹ (A_g), 497 cm⁻¹ (B_g), 532 cm⁻¹ (B_g), 555 cm⁻¹ (A_g), 612 cm⁻¹ (B_g), and 632 cm⁻¹ (A_g), and the absence of discernible *t*-ZrO₂ signals.^[70–72] It can be therefore concluded that the annealing at 600 and 750 °C yields *t*-ZrO₂, whereas the thermal treatment at 1050° and 1200 °C results in *m*-ZrO₂. At 900 °C, a partly transformed product containing mostly *t*-ZrO₂ and trace *m*-ZrO₂ is synthesized.

The influence of annealing on the crystallinity of the resin-derived ZrO₂ powders is investigated using confocal Raman spectroscopy and X-ray powder diffraction (XRD) to cross-validate the results found for the 3D-ZrO₂ structures analyzed with Raman. The resin is cured using a conventional 36 W UV lamp (Figure 1b). The portions of polymerized resin are pulverized in an agate mortar and annealed for 1 h at 600, 750, 900, 1050, and 1200 °C (Figure 1d). The XRD results (Figure 3b) for samples annealed at 600 and 750 °C give a characteristic *t*-ZrO₂ (P4₂/nmc space group) diffractogram with dominant (101) diffraction at 30.3°.^[75–77] Partly transformed zirconia containing ≈76% of *m*-ZrO₂ phase is yielded after treatment at 900 °C (Figure S5, Supporting Information), confirmed by the presence of (111) *t*-ZrO₂ diffraction at 30.3° and emergence of the distinctive *m*-ZrO₂ peaks at 28.3° (111) and 31.5° (111).^[76] The annealing at 1050 and 1200 °C results in the complete

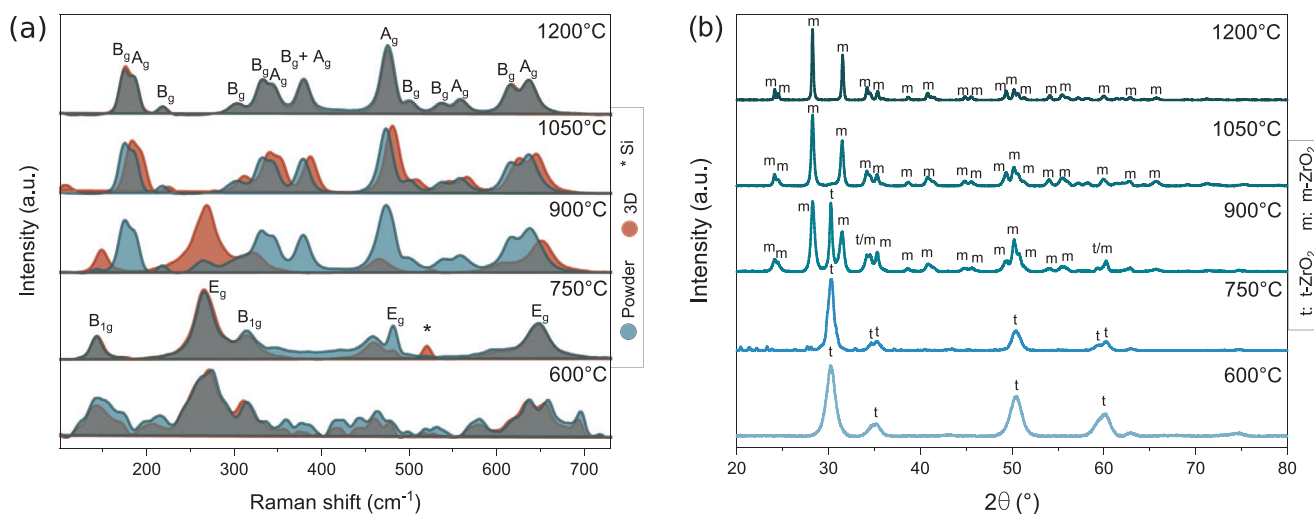


Figure 3. a) Confocal Raman spectroscopy spectra of 3D-printed ZrO₂ structures annealed at 600, 750, 900, 1050, and 1200 °C for 1 h; samples excited at 532 nm. Labels: blue – powders, red – 3D structures. B_{1g} and E_g are *t*-ZrO₂ vibrational modes, and B_g and A_g *m*-ZrO₂. Asterisk (*) denotes the Si substrate signal. b) XRD diffractograms for ZrO₂ powders obtained from pulverized UV-cured Zr-rich resin annealed at 600, 750, 900, 1050, and 1200 °C for 1 h. Labels: t for *t*-ZrO₂, m for *m*-ZrO₂.

transformation to $m\text{-ZrO}_2$ ($P2_1/c$ space group).^[78] No phase lines typical for discernible impurities, $t\text{-ZrO}_2$, $c\text{-ZrO}_2$, or oxygen-deficient ZrO_2 , are observed.^[76]

For confocal Raman spectroscopy, the powder samples are cast on a 10×10 mm sapphire substrate and characterized with a 532 nm excitation laser. The spectroscopic results obtained for powders and ZrO_2 3D structures are in good agreement (Figure 3a, labeled in blue). Similar phase transformation temperatures for the 3D-printed ZrO_2 structures have been found for powders and layers obtained from carbon-rich mixtures via a sol-gel process^[79,80] or for electrospun nanofibers.^[75,81] To this end, 3D-printed $t\text{-ZrO}_2$ samples annealed at 600 and 750 °C and the 3D-printed $m\text{-ZrO}_2$ treated at 1050 and 1200 °C are comparable to the powder ZrO_2 . From these results, it is fair to say that confocal Raman spectroscopy and XRD help to cross-compare the results of the 3D-printed ZrO_2 structures.

The intrinsic luminescent properties of the $t\text{-ZrO}_2$ and $m\text{-ZrO}_2$ are studied with CL for representative buckyballs annealed at 600 and 1200 °C. Powders obtained from the resins under the same annealing conditions are used as references. Figure 4a,e shows SEM and panchromatic CL images of a ZrO_2 buckyball, thermally treated at 600 °C. All regions of the 3D structure generate luminescence in agreement with its high crystallinity. Furthermore, images acquired at high magnifications reveal a grain structure in the ZrO_2 buckyballs, as shown in Figure 4e,f, with some grains exhibiting a low CL intensity (see arrows) that we attribute to a low density of radiative centers. Point defects, such as oxygen vacancies (V_O), typically act as radiative centers in $t\text{-ZrO}_2$,^[82] which could be present at low density in some grains of buckyballs. CL images obtained from a ZrO_2 buckyball annealed at 1200 °C reveal a similar CL distribution, as shown in Figure 4c,d,g,h.

CL spectra obtained from ZrO_2 buckyballs thermally treated at 600 and 1200 °C show broad emissions centered at about 2.9 and 2.6 eV, composed of several components as shown in Figure 4i,j. The components calculated by the deconvolution of the CL spectra using Gaussian curves are centered at 1.65, 2.3, 2.6, 2.9, 3.2, and 3.5 eV for ZrO_2 annealed at 600 °C and centered at 2.3, 2.6, and 2.9 eV for ZrO_2 buckyballs annealed at 1200 °C, to match the energy of defects-related emissions reported by other authors.^[79,83–86] The full width at half maximum (FWHM) of these components is adjusted to obtain a fitting value for the coefficient of determination nearest to unity. The values obtained for this parameter are 0.995 and 0.997 after fitting the CL spectra of ZrO_2 buckyballs annealed at 600 and 1200 °C by assigning an FWHM of 0.35 eV to each Gaussian component. It is essential to consider that the FWHM usually simultaneously represents the homogeneous and inhomogeneous broadening of the linewidth of an electronic transition. Electron–phonon coupling in perfect crystals generates the homogeneous or natural broadening (represented with a Lorentzian curve). In contrast, the inhomogeneous broadening (commonly represented with a Gaussian curve) is generated by crystallinity disorder associated with impurities, anti-site defects, or vacancies.^[87,88] In this work, we have assigned the same FWHM value of 0.35 eV for all defect-related emissions in ZrO_2 buckyballs, attributing that each corresponds to individual electronic transition with a comparable inhomogeneous

broadening. The component of 3.5 eV has been reported by Cong et al.,^[83] proposing an origin to electronic transitions from excited (F^+)^{*} centers and the valence band (VB). An oxygen vacancy (V_O) physically represents a well-potential of finite height into a crystal with quantized energy levels that one or two electrons can occupy. An F^+ center is an oxygen vacancy (V_O) with a single trapped electron in such well-potential occupying the ground-state energy and exhibiting an s -like wave function, which can be promoted to the first excited state to exhibit a p -like wave function. This last excited state is known as an excited (F^+)^{*} center.^[89,90] Electrons trapped in V_O states can recombine with holes to generate electromagnetic radiation or remain in the lattice modifying its charge distribution. For example, Kumar et al. previously reported that Zr^{4+} ions abutting bulk V_O could capture electrons forming Zr^{3+} species.^[91] The band of 3.2 eV has been reported by Wang et al. in $t\text{-ZrO}_2$ nanopowders, associating its generation to the presence of F^+ centers.^[84] For the component of 2.9 eV, Lin et al. have demonstrated by electronic paramagnetic resonance (EPR) measurements that its origin is due to the presence of carbon impurities as interstitial defects (C_i) in $t\text{-ZrO}_2$ powders, besides that the formation of V_O in the lattice of $m\text{-ZrO}_2$ generates the 2.6 eV emission.^[79] However, emission of 2.6 eV also has been reported in $m\text{-ZrO}_2$ powders by Ashraf et al., proposing an origin to electronic transitions between the levels generated by the excited F^{+*} and F^+ states.^[85] Finally, the component of 2.3 eV could correspond with the emission of 2.2 eV for $t\text{-ZrO}_2$ nanoparticles reported by Zhang et al. They attribute it to the presence of carbon impurities (C_i), demonstrating that the emission is tuned in energy with the amount of carbon incorporated in such nanostructures.^[86] The additional monochromatic CL images of $t\text{-ZrO}_2$ and $m\text{-ZrO}_2$ buckyballs obtained at 2.6 and 2.9 eV are provided in Figure S6 (Supporting Information). The presence of carbon-based impurities is highly probable for polymer-derived ceramics^[56] and has been previously observed for ZnO microstructures fabricated via TPL.^[55] Figure 4j reveals that CL emission from $m\text{-ZrO}_2$ buckyballs only exhibits the components of 2.3, 2.6, and 2.9 eV, where the second dominates the spectrum and can be associated with the presence of carbon impurities (C_i). The absence of the 3.2 and 3.5 eV emissions in $m\text{-ZrO}_2$ buckyballs indicates that thermal treatment at 1200 °C does not eliminate carbon impurities (C_i) but suppresses V_O point defects. Lin et al. have computed structural models of carbon impurities (C_i) in $t\text{-ZrO}_2$ and oxygen vacancies (V_O) in $m\text{-ZrO}_2$, considering that they are present in each of these phases. They demonstrate that the bandgap of $t\text{-ZrO}_2$ with C_i is slightly larger than that of $m\text{-ZrO}_2$ with V_O .^[79] In accordance with these results, we conclude that 3D silicon-free $t\text{-ZrO}_2$ buckyballs contain V_O and C_i point-defects and that $m\text{-ZrO}_2$ buckyballs contain C_i point-defects predominantly. To confirm that the fabrication of ZrO_2 buckyballs does not generate new point defects other than the ones typically observed in ZrO_2 , we acquired CL spectra from undoped ZrO_2 powders thermally treated at the same temperatures as ZrO_2 buckyballs. Figure 4k,l depict CL spectra from undoped ZrO_2 powders annealed at 600 and 1200 °C, revealing the same CL components found in $t\text{-ZrO}_2$ and $m\text{-ZrO}_2$ buckyballs attributed to the presence of oxygen vacancies and carbon impurities.

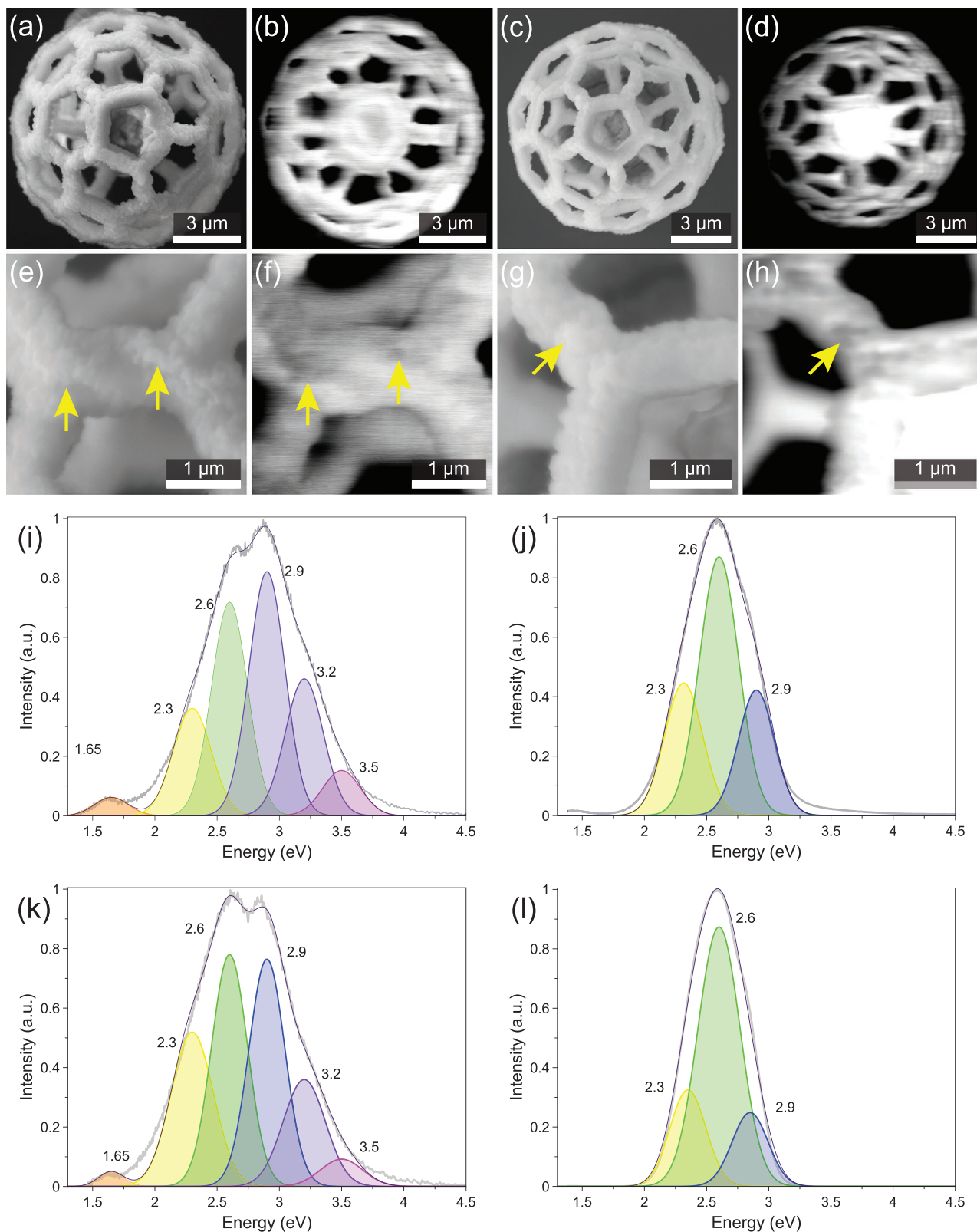


Figure 4. a) SEM and e) panchromatic CL images of an undoped ZrO_2 buckyball thermally treated at 600 °C. b) SEM and f) CL images of the grain structure reveal an inhomogeneous luminescence. c) SEM and g) panchromatic CL images of an undoped ZrO_2 buckyball thermally treated at 1200 °C. d) SEM, h) panchromatic CL image. Scale bars represent (a–d) 3 μm and (e–h) 1 μm . Deconvoluted normalized CL spectra of the undoped i) t - ZrO_2 and j) m - ZrO_2 buckyballs thermally treated at 600 and 1200 °C. Deconvoluted CL spectra of the undoped k) t - ZrO_2 and l) m - ZrO_2 powders thermally treated at 600 and 1200 °C.

2.2. Additive Manufacturing of Eu-Doped *t*-ZrO₂ and *m*-ZrO₂ Luminescent Microarchitectures

After successfully fabricating *t*-ZrO₂ and *m*-ZrO₂ 3D-structures, we investigate the possibility of doping with Eu³⁺ by adding europium acetate hydrate (EuOAc × H₂O) to the resin (3 mol% of Eu, relative to Zr). First, the influence of doping on the crystallographic phase of ZrO₂:Eu powders derived from the UV-cured resin annealed at 600 and 1200 °C is studied using XRD (Figure S7, Supporting Information). We conclude that, at least for the tested concentrations, doping with Eu does not alter the resulting crystallographic phases of ZrO₂ or yield in a different product. Characteristic *t*-ZrO₂ pattern with dominant (101) *t*-ZrO₂ reflection at 30.3° for the powder thermally treated at 600 °C is preserved.^[75,76] For the sample annealed at 1200 °C a distinctive *m*-ZrO₂ diffractogram with the most intense peaks at 28.3° (111) and 31.5° (111) is observed.^[76] The Eu content estimated via EDS is 3.4% wt. (Zr 26.1, O 71, C 4.0% wt). The presence of carbon impurities in powder samples reinforces the conclusions on their influence on observed emissions for *t*-ZrO₂ and *m*-ZrO₂. X-ray photoelectron spectroscopy (XPS) analysis is assessed to confirm the chemical state of Eu (Figure S8, Supporting Information). The oxidation state of the dopant in ZrO₂ powder annealed at 1200 °C is predominantly Eu³⁺. A small amount of Eu²⁺ is found, which potential origin is discussed below.

Next, ZrO₂:Eu³⁺ 3D-structures are manufactured via TPL following the same protocol as for ZrO₂ (Figure 1a'). The developed, printed buckyballs are annealed at 600 and 1200 °C for 1 h. Figure 5a–f shows SEM and CL images obtained for the point-defect (2.9 and 2.6 eV) and Eu³⁺ ions (2.1 eV) emissions for *t*-ZrO₂:Eu³⁺ and *m*-ZrO₂:Eu³⁺ buckyballs. These images reveal a homogeneous CL distribution for the V_O-related 2.9 eV emission (Figure 5b) and C_i-related 2.6 eV (Figure 5f) emission in *t*-ZrO₂:Eu³⁺ and *m*-ZrO₂:Eu³⁺ buckyballs, respectively. In addition, brighter regions at the edges of the buckyballs for the Eu³⁺ emission of 2.1 eV (Figure 5c,f) reveal that the dopant is mainly present at the edges of such 3D structures. This contrast could also be ascribed to a more intense CL emission associated with the higher specific free surface of the buckyball at the edges; however, since this effect is not observed in the CL images obtained at 2.9 and 2.6 eV (Figure 5b,e), we conclude that the CL image obtained at 2.1 eV represents the Eu³⁺ distribution. Figure 5i,j shows CL spectra from *t*-ZrO₂:Eu³⁺ and *m*-ZrO₂:Eu³⁺ buckyballs, exhibiting strong emissions generated by transitions between levels ⁵D₀ and ⁷F₁ of Eu³⁺. CL spectrum of the *t*-ZrO₂:Eu³⁺ buckyball also shows a weak broad emission with components of 2.6, 2.9, 3.2, and 3.5 eV (Figure 5i), suggesting that Eu³⁺ ions incorporated as a substitutional impurity (Eu_{Zr}) in the *t*-ZrO₂ lattice without modifying its defect structure. Furthermore, Figure 5j also reveals that Eu³⁺ ions incorporated in the *m*-ZrO₂ quench the emissions associated with point-defects (inset in Figure 5j). CL measurements obtained from ZrO₂:Eu³⁺ powders also reveal electronic transitions corresponding with Eu³⁺ ions for tetragonal and monoclinic phases, as shown in Figure 5k,l. In contrast to ZrO₂:Eu³⁺ buckyballs, the *m*-ZrO₂:Eu³⁺ powders revealed an increase in the emission intensity of 2.3, 2.6, and 2.9 eV, suggesting that the fabricated *m*-ZrO₂:Eu³⁺ buckyballs possibly contain fewer

oxygen vacancies. However, we do not discard the possibility that the increase of the intensity of these three bands could also be correlated with a partial reduction of Eu³⁺ species to Eu²⁺ in the *m*-ZrO₂:Eu³⁺ powder because the Eu²⁺ signals generated by electronic transitions between the levels 4f₆5d₁ and 4f₇(⁸S_{7/2}) can overlap with peaks typically observed for the luminescence of intrinsic ZrO₂ defects within the 3.18–2.38 eV range.^[92] These findings may correspond with small quantities of Eu²⁺ observed in the XPS results for *m*-ZrO₂:Eu³⁺ powder (Figure S8d, Supporting Information), not observed in the Eu-doped *m*-ZrO₂ buckyballs. The reduction of Eu³⁺ to Eu²⁺ can be readily induced in organic solvents by femtosecond laser radiation and UV light.^[93,94] In practice, the extent to which resin curing affects the Eu²⁺ population seems limited. In our study, CL emissions are related to Eu²⁺ species observed in Eu-doped *m*-ZrO₂ powder. The Eu²⁺ formation likely proceeds during the thermal processing. Various mechanisms have been discussed for the Eu³⁺ reduction to Eu²⁺ in mixed oxide host matrices.^[95] We propose that the reduction of Eu³⁺ in *m*-ZrO₂ powder may proceed from the defect centers during annealing.^[96] Upon increasing the annealing temperature in the air from 600 to 1200 °C, the V_O population reduces, which indirectly indicates they may participate in the Eu²⁺ formation. Although our work is dedicated to 3D printing ZrO₂:Eu structures, it is also a pioneer in using photopolymerization and metal–organic monomers to obtain bulk powders. Further dedicated studies on powder phosphors derived from the carbon-rich precursors should help better interpret the Eu³⁺ reduction phenomenon.

Finally, the optical emission of the representative *m*-ZrO₂:Eu³⁺ buckyball is investigated with wide-field fluorescence microscopy. The 3D structure is excited using a 405 nm source resulting in orange-red emission (Figure 5g), a color that agrees with the transitions between levels ⁵D₀ and ⁷F₁ of Eu³⁺ observed with CL. The uniformity of the emission from the 3D phosphor in the lateral direction is assessed (Figure 5h), showing a pattern resembling the morphology of the buckyball. A 3D reconstruction of the 3D structure is presented in Video S2 (Supporting Information).

3. Conclusions

We have manufactured 3D silicon-free ZrO₂ microstructures with sub-micrometer feature sizes for the first time. The influence of the annealing temperature (600, 750, 900, 1050, 1200 °C) was studied using XRD and Raman. The presented method yields *t*-ZrO₂ and *m*-ZrO₂ architectures. The microstructures undergo ≈60% isotropic shrinkage after annealing, compared to the initial dimensions of the printed pre-ceramic architectures. With the increase of the annealing temperature, the gradual growth of the grains building the microstructures is observed with the aid of SEM, as expected on the premise of XRD peak narrowing for the reference powders. The cathodoluminescence study reveals a broadband emission in the 1.65–3.5 eV range for *t*-ZrO₂ and within the 2.3–2.9 eV for *m*-ZrO₂, which unveils the lattice structure of *t*-ZrO₂ contains oxygen vacancies and carbon impurities, while *m*-ZrO₂ predominantly the latter ones.

The developed resin is compatible with europium acetate hydrate, used as a dopant to introduce 3.4 wt% of Eu³⁺ into

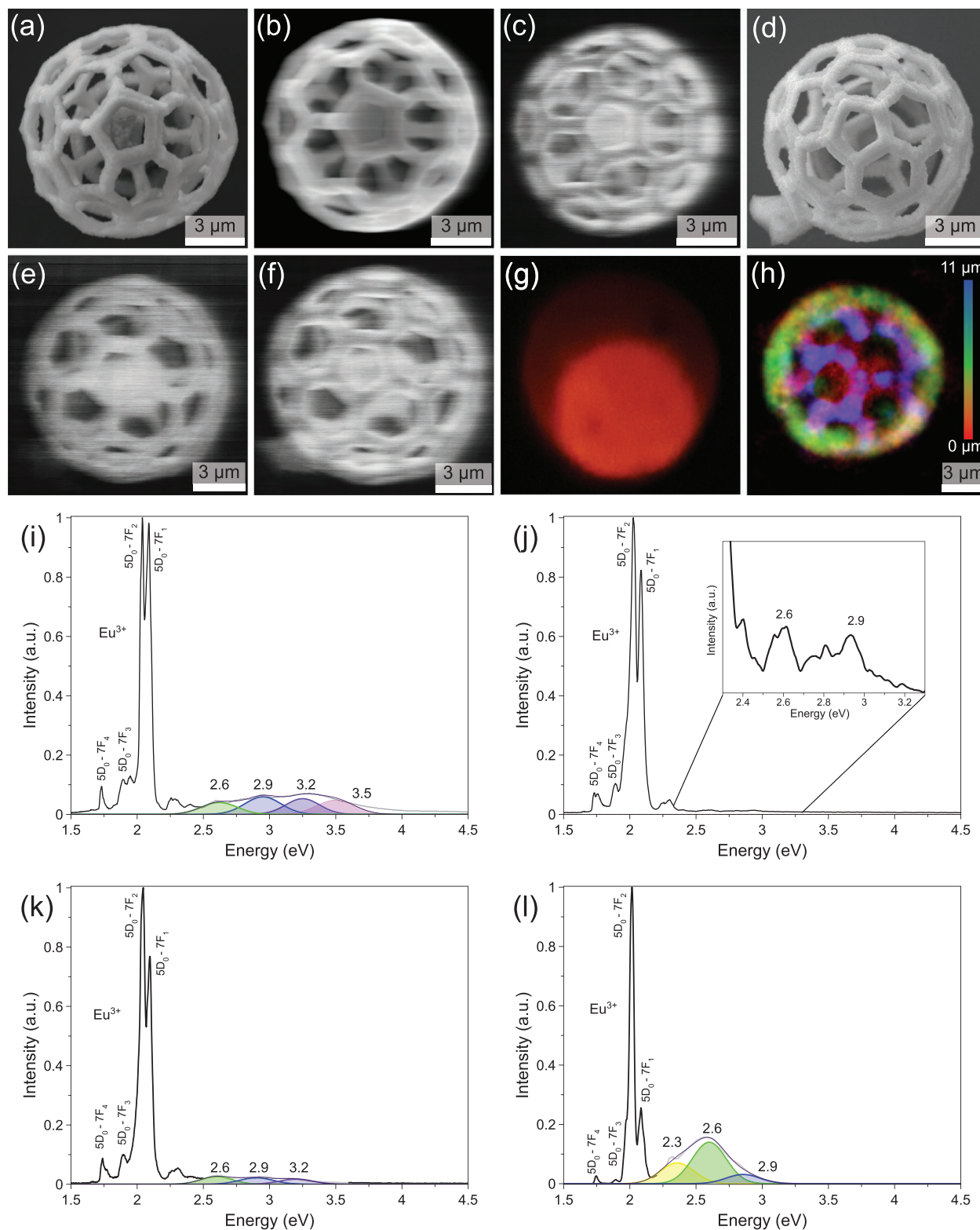


Figure 5. a) SEM and monochromatic CL images obtained at b) 2.9 eV and c) 2.1 eV of a $\text{ZrO}_2:\text{Eu}^{3+}$ buckyball thermally treated at 600 °C. d) SEM and monochromatic CL images obtained at e) 2.6 eV and f) 2.1 eV of a $\text{ZrO}_2:\text{Eu}^{3+}$ buckyball thermally treated at 1200 °C. Scale bars represent 2 μm . g) Digital camera image showing orange-red emission from the $m\text{-ZrO}_2:\text{Eu}^{3+}$ buckyball upon excitation at 405 nm, collected from the microscope eyepiece. h) Color-coded z-stack image of the $m\text{-ZrO}_2:\text{Eu}^{3+}$ buckyball emission upon excitation at 405 nm; color scale: blue corresponds with the emission from the top, green from the middle, and red from the bottom of the buckyball; scale bar represents 3 μm . Normalized CL spectra of the Eu-doped ZrO_2 buckyballs thermally treated at i) 600 °C and j) 1200 °C revealing a quenching of the point defect bands. Deconvoluted CL spectra of the Eu-doped ZrO_2 powders thermally treated at k) 600 °C and l) 1200 °C.

the ZrO₂ matrix. The doping of ZrO₂ with Eu does not affect the resulting crystallographic phase of ZrO₂; fabrication of *t*-ZrO₂:Eu³⁺ and *m*-ZrO₂:Eu³⁺ microstructures is feasible with the presented approach. The 3D-printed ZrO₂:Eu³⁺ buckyballs annealed at 600 and 1200 °C are highly efficient phosphors. Interestingly, Eu³⁺ is localized mainly at the edges of these 3D structures, which can be observed as brighter regions in the CL images obtained at 2.1 eV, corresponding with the characteristic Eu³⁺ emission. The emission properties of the buckyballs and ZrO₂:Eu³⁺ powders are characteristic for the material and in agreement with previously reported components. The *t*-ZrO₂:Eu³⁺ buckyball emissions are dominated with ⁵D₀₋₇F₁ and ⁵D₀₋₇F₂ transitions; in the case of the *m*-ZrO₂:Eu³⁺ structure, the latter one is subtly less intense. Upon doping, the defect structure of the *t*-ZrO₂ lattice results in a weak broad emission with components of the 2.6–3.5 eV range. Accordingly, the *m*-ZrO₂ matrix quenches the emissions associated with the point defects. Both *t*-ZrO₂:Eu³⁺ and *m*-ZrO₂:Eu³⁺ buckyballs show additional weak ⁵D₀₋₇F₃ and ⁵D₀₋₇F₄ transitions. Finally, upon excitation of the *m*-ZrO₂:Eu³⁺ buckyball with 405 nm light, orange-red emission, homogenous in the lateral dimension of the architecture, is observed.

TPL allows manufacturing features emitting in the visible range, with sizes practically impossible to resolve with the naked eye. The optical properties of lanthanide-based phosphors are not limited to orange-red emission of Eu³⁺ and can be leveraged to produce white emission.^[97] From a broad perspective, we envision that our AM approach will contribute to the current trend of extreme dimensional refinement of materials, prospectively marrying materials science with optoelectronics. Due to the heat buildup in the phosphor-based light-emitting devices, the population of electronically excited states may significantly diminish through the nonradiative relaxation processes.^[98] As a result, both the emission intensity and color may change, which in practice limits the range of commercially applied phosphor light-emitting devices.^[98] Various strategies of thermal quenching mitigation have been discussed in the literature, i.e., encapsulation in glass, application of coatings, increasing cation order, or modification of defect levels.^[99] With 3D-structuring at the microscale, additional active or passive cooling could be introduced to improve heat dissipation.^[100] In addition, the presented structuring methodology could help to increase the resolution and efficiency of arrayed phosphor light sources. The spatial separation of precisely positioned 3D-printed pixels could be tuned to limit the detrimental optical crosstalk through the reduced light scattering.^[100]

Such hierarchical, structured photoluminescent materials offer a plethora of uses, for example, in 3D light guiding,^[101] sensing,^[102] or the preparation of fraud-resistant labels.^[97,103] The prospective application areas for the 3D phosphor microstructures are integrated optics, lightning sources, and light-emitting diodes.^[104–106] Understanding the correlation between the 3D structuring, radiative thermal transfer, and the performance of phosphors could help further optimize the phosphor-based light-emitting technologies. The formulation of next-generation less-invasive surgical equipment may likely rely on the level of miniaturization and integration that, as presented, can be achieved via two-photon lithography. Owing to the biocompatibility of ZrO₂,^[107] phosphors based on such

lanthanide host matrix could be, e.g., integrated into biomedical imaging devices.^[108]

4. Experimental Section

Materials: Dichloromethane (anhydrous, ≥99.8%, containing 40–150 ppm amylene as a stabilizer), N,N-dimethylacetamide (anhydrous, 99.8%), pentaerythritol triacrylate (technical grade), and zirconium acrylate were purchased from Sigma-Aldrich. Acrylic acid (99%, stabilized with ≈200 ppm 4-methoxyphenol), DMSO (>99%), and europium (III) acetate hydrate (99.99%) were acquired from Alfa Aesar. DETC (97%) was purchased from J&K Scientific. IPA (for analysis EMSURE ACS, ISO, Reag. Ph Eur) was obtained from Supelco. All chemicals were used as received without further purification.

Zirconium-Containing Resin: ZrA (75 mg) was placed in a 50 mL pear-shaped amber glass flask, to which AA (150 mg), DMAc (500 mg), and DCM (2 g) were added. The flask was attached to a rotary evaporator equipped with a water bath set at 40 °C, and the contents were rotated at 150 rpm under ambient pressure for one hour until the complete dissolution of zirconium acrylate. PETA (300 mg) was added, and the mixing continued for an additional 60 min, after which DETC (23 mg) and DCM (100 mg) were added. The rotation-mixing was continued for 30 min, DCM was then removed under reduced pressure at 40 °C and 180 rpm, confirmed by gravimetric analysis. The product was placed in an amber glass vial to cool down and degas before use. Complete dissolution of solid materials was assured by inspection of a drop-casted droplet on a silicon wafer dice under an optical microscope equipped with 100×/0.9 objective. After 24 h of storage at room temperature, no precipitation was observed in the resin. All preparations and further experiments were conducted in yellow light to prevent premature crosslinking of the resin.

Europium-Doped Zirconium-Containing Resin: Briefly, europium (III) acetate hydrate (EuAc × H₂O) (1.65 mg) was added to ZrA (75 mg). The same later steps were followed as for zirconium-containing resin.

Two-Photon Lithography: Metal–organic polymeric structures were fabricated using a commercial two-photon lithography system (Photonic Professional GT, Nanoscribe) equipped with a differential interference contrast 63×/1.4 NA oil immersion objective (Plan-Apochromat, Carl Zeiss). Immersion oil (Immersion 518 F, Carl Zeiss) was applied on the bottom side of the glass coverslip (30 mm diameter, 170 μm thickness) fixed in the sample holder with rubber cement. On the top side, a droplet of the organic–inorganic resin was drop-casted between two parallel ribbons of polyimide film tape (3 mm width, 12 mm length, 100 μm thickness) later covered with a 1 × 1 cm silicon wafer dice on which the 3D objects were printed (Figure 1b) using reflection mode. Laser power of 18.9 mW and 1 mm s⁻¹ scanning speed was applied. The printed structures were developed in DMSO for 10 min and in IPA for 2 min and later dried at 65 °C for 12 h before annealing.

Pulverized UV-Cured Resins: The organic–inorganic resins were poured onto a petri dish to form a thin layer, then crosslinked using a commercial 36W halogen ultraviolet curing lamp (EBN001, Esperanza) for 180 min. The formed metal–organic polymer was pulverized in an agate mortar and dried in a furnace (Binder, Model ED 23) at 80 °C overnight to remove the residual DMAc.

Thermal Processing: Based on the thermogravimetric analysis (TGA) (Figure S9, Supporting Information), most of the organic constituents of the resin were readily combusted below 500 °C. Thus, a two-step thermal annealing in the air was adopted in the study. The silicon substrates on which the 3D structures were printed and the pulverized UV-cured resins were placed in crucibles to be ceramized in the air at ambient pressure via a two-stage heating process using a chamber furnace (LH 15/12, Nabertherm). A heating profile of 1 °C min⁻¹ was applied to reach 500 °C, after which the increased 2 °C min⁻¹ rate was set to attain the target temperature (600, 750, 900, 1050, and 1200 °C) maintained for 60 min. The samples were allowed to cool down at the natural rate to room temperature.

Cathodoluminescence: Room temperature CL measurements were conducted using a JEOL JIB-4500 SEM equipped with a Gatan MonoCl4 detector. An acceleration voltage of 15 kV was applied.

Confocal Raman Spectroscopy (Raman): Raman spectra were obtained using a confocal Raman microscopy system (Alpha 300, WiTec) equipped with a 100×/0.9 NA air objective (MPlan FL N, Olympus) and 532 nm excitation laser set at 5.0 mW power. Selected samples were additionally excited with 633 and 785 nm lasers at 5.0 mW power. Registered data consist of 30 averaged spectra, each accumulated for 10 s in backscattering geometry using a 600 g mm⁻¹ grating. The data were processed using CrystalSleuth software to remove cosmic rays and reduce background. For 3D-printed structures, additional Si substrate spectra were recorded for each annealing temperature (Figure S4, Supporting Information). The powders obtained from the annealed resins were ground in an agate mortar and characterized on the sapphire substrates.

Wide-Field Fluorescence Microscopy: The sample was positioned facing the objective and mounted on a coverslip (100 μm thickness, 24 mm diameter) with double-sided tape as a spacer. A drop of immersion oil (Nikon) was used between the objective and the coverslip. Micrographs were recorded using a Nikon Eclipse Ti inverted microscope equipped with a Nikon SR Apo TIRF 100× 1.49 NA oil immersion objective coupled with Andor iXon Ultra 897 camera set at 50 ms exposure time and 50 EMCCD gain. A 405 nm laser (Oxxius) with 800 W cm⁻² irradiance was used for the excitation. The emitted light was separated from the excitation using a quad-band 405/488/561/647 nm dichroic mirror and filtered with the matching fluorescence filter (Semrock). Each camera pixel corresponded to 107 nm in the object plane. The z displacement was provided by a piezoelectric nanopositioner (Nano-Z, Mad City Labs). For each 250 nm mechanical step, four frames were acquired and averaged. The images were processed to reduce the focal shift of the z positions due to the index mismatch, assuming the 0.5 value.^[109] A Python code was written to reduce off-focus background by subtracting the local mean value for each frame with 15-pixel Gaussian sigma. The multicolor image was generated with Fiji software by superposing depth color-coded images at various z planes. Finally, the 3D movie was generated with the Fiji 3D Viewer. It should be noted that the image presenting orange-red emission from the *m*-ZrO₂:Eu³⁺ buckyball excited at 405 nm (Figure 5g) was collected directly from the ocular lens aperture of the fluorescence microscope using a smartphone due to the lack of an RGB camera.

SEM and SEM-EDS: The top-view images of 3D structures were recorded using SEM (Carl Zeiss, Merlin AURIGA CrossBeam Workstation) equipped with Inlens and High-Efficiency Secondary Electron (HE-SE2) detectors. An acceleration voltage of 1.5–2.2 kV was applied. The description of the image processing for display purposes is provided (Figure S10, Supporting Information). Elemental mappings were prepared using an EDS attachment to the SEM system. The data were processed with AZtec (Oxford Scientific) software.

Thermogravimetric Analysis: The weight losses of the cured dried resin placed in platinum crucible were analyzed at a 5 °C min⁻¹ heating rate in the air within a 37–1200 °C range (STA 449 F3, Netzsch).

Tomography: A FIB/SEM dual-beam microscope (Thermo Fisher Scientific, Helios Nanolab 600i) was used for the tomography of the octet-truss lattice. The tomography consists of 139 slices with a spacing of ≈80 nm. Milling of the single slices was performed at 30 kV acceleration voltage and with a beam current of 230 pA. The single slices were recorded with a secondary electron detector at an acceleration voltage of 5 kV and a beam current of 0.69 nA. The images were aligned via digital image correlation (DIC) by the microscope software Auto Slice and View 4.0 (Thermo Fisher Scientific).

X-Ray Powder Diffraction: The samples of annealed cured resins were cast on a zero-diffraction plate and characterized with a diffractometer (D2 Phaser, Bruker) (30 kV, 10 mA) equipped with LynxEye detector, using Cu-Kα source radiation at 2θ scan range of 20°–80° with 2.25° min⁻¹ scan speed. The spectra were baseline-corrected using CrystalSleuth software.

X-ray Photoelectron Spectroscopy: XPS measurements were conducted with a SPECS system equipped with a PHOIBOS WAL analyzer using

an Al anode. High-resolution spectra were obtained using 300 scans at 0.1 eV sensitivity. Eu-doped *m*-ZrO₂ powder was quantified with the aid of CasaXPS processing software, and XPS spectra were deconvoluted into Gaussian peaks using a Shirley background. The obtained spectra were calibrated using the C 1s signal (284.6 eV) as reference.

Supporting Information

Supporting Information is available from the Wiley Online Library or from the author.

Acknowledgements

The authors appreciate the help of Mark Smithers in performing the high-resolution SEM and SEM-EDS imaging. The authors thank Cindy Huiskes for conducting the TGA. The authors thank D. Dominguez for conducting the XPS characterization. J.P.W. received a University of Twente Graduate School bridging grant. J.P.W., A.S.-A., and H.G. received funding from the European Research Council (ERC) under the Horizon 2020 research and innovation programme of the European Union under Grant Agreement No. 742004. This research used the Live Cell Imaging Facility resources at the University of Twente (UT). S.G. and B.M.'s contribution to this project received funding from the European Research Council (ERC) under the European Union's Horizon 2020 research and innovation programme (Grant No. 949626). M.H. received funding from the University of California Institute for Mexico and The United States (UCMEXUS) (No. CN19137) and CONACYT (Grant No. 284667).

Conflict of Interest

The authors declare no conflict of interest.

Data Availability Statement

The data that support the findings of this study are available from the corresponding author upon reasonable request.

Keywords

additive manufacturing, europium, luminescence, two-photon lithography, zirconia

Received: December 17, 2021

Revised: March 17, 2022

Published online:

- [1] J.-C. G. Bünzli, *Trends Chem.* **2019**, *1*, 751.
- [2] Q. Ma, J. Wang, Z. Li, X. Lv, L. Liang, Q. Yuan, *Small* **2019**, *15*, 1804969.
- [3] C. Cheng, L. Ning, X. Ke, M. S. Molokeev, Z. Wang, G. Zhou, Y. C. Chuang, Z. Xia, *Adv. Opt. Mater.* **2020**, *8*, 1901608.
- [4] C. D. S. Brites, S. Balabhadra, L. D. Carlos, *Adv. Opt. Mater.* **2019**, *7*, 1801239.
- [5] X. Kang, C. Li, Z. Cheng, P. Ma, Z. Hou, J. Lin, *Wiley Interdiscip. Rev. Nanomed. Nanobiotechnol.* **2014**, *6*, 80.
- [6] L. Jin, Y. Wu, Y. Wang, S. Liu, Y. Zhang, Z. Li, X. Chen, W. Zhang, S. Xiao, Q. Song, *Adv. Mater.* **2019**, *31*, 1807079.

- [7] X. Chen, T. Sun, F. Wang, *Chem. - Asian J.* **2020**, *15*, 21.
- [8] X. Chen, in *Lanthanide-Doped Luminescent Nanomaterials* (Eds: X. Chen, Y. Liu, D. Tu), Springer-Verlag, Heidelberg, Germany **2014**, pp. 1–16.
- [9] M. H. V. Werts, *Sci. Prog.* **2005**, *88*, 101.
- [10] S. Moynihan, D. Iacopino, D. O'Carroll, H. Doyle, D. A. Tanner, G. Redmond, *Adv. Mater.* **2007**, *19*, 2474.
- [11] S. Kalaivani, S. Kannan, *J. Biomed. Mater. Res., Part B* **2020**, *108*, 2656.
- [12] A. Patra, C. S. Friend, R. Kapoor, P. N. Prasad, *J. Phys. Chem. B* **2002**, *106*, 1909.
- [13] P. Vařák, J. Mrázek, W. Blanc, J. Aubrecht, M. Kamrádek, O. Podrazký, *Opt. Mater. Express* **2020**, *10*, 1383.
- [14] J. Lægsgaard, *Phys. Rev. B* **2002**, *65*, 174114.
- [15] A. Ćirić, S. Stojadinović, *J. Alloys Compd.* **2020**, *832*, 154907.
- [16] L. X. Lovisa, J. Andrés, L. Gracia, M. S. Li, C. A. Paskocimas, M. R. D. Bomio, V. D. Araujo, E. Longo, F. V. Motta, *J. Alloys Compd.* **2017**, *695*, 3094.
- [17] T. Smith, J. Guild, *Trans. Opt. Soc.* **1931**, *33*, 73.
- [18] C. Tiseanu, B. Cojocaru, V. I. Parvulescu, M. Sanchez-Dominguez, P. A. Primus, M. Boutonnet, *Phys. Chem. Chem. Phys.* **2012**, *14*, 12970.
- [19] S. Manjunatha, R. Hari Krishna, T. Thomas, B. S. Panigrahi, M. S. Dharmaparakash, *Mater. Res. Bull.* **2018**, *98*, 139.
- [20] S. D. Meetei, S. D. Singh, *J. Lumin.* **2014**, *147*, 328.
- [21] A. Mondal, S. Ram, *J. Am. Ceram. Soc.* **2008**, *91*, 329.
- [22] E. Hemmer, K. Soga, T. Konishi, T. Watanabe, T. Taniguchi, S. Mathur, *J. Am. Ceram. Soc.* **2010**, *93*, 3873.
- [23] T. Ninjbadgar, G. Garnweitner, A. Boärger, L. M. Goldenberg, O. V. Sakhno, J. Stumpe, *Adv. Funct. Mater.* **2009**, *19*, 1819.
- [24] H. Zhang, X. Fu, S. Niu, G. Sun, Q. Xin, *Mater. Chem. Phys.* **2005**, *91*, 361.
- [25] M. Wang, X. Wang, J. Lin, X. Ning, X. Yang, X. Zhang, J. Zhao, *Ceram. Int.* **2015**, *41*, 8444.
- [26] S. Lange, V. Kiisk, J. Aarik, M. Kirm, I. Sildos, *Phys. Status Solidi C* **2007**, *4*, 938.
- [27] X. Qu, H. Song, G. Pan, X. Bai, B. Dong, H. Zhao, Q. Dai, H. Zhang, R. Qin, S. Lu, *J. Phys. Chem. C* **2009**, *113*, 5906.
- [28] R. Rejsfeld, T. Saraidarov, M. Pietraszkiewicz, S. Lis, *Chem. Phys. Lett.* **2001**, *349*, 266.
- [29] A. B. Suryamas, M. M. Munir, T. Ogi, C. J. Hogan, K. Okuyama, *Jpn. J. Appl. Phys.* **2010**, *49*, 115003.
- [30] J. Huang, P. Wu, *Nano-Micro Lett.* **2021**, *13*, 15.
- [31] Y. Yao, C. Yin, S. Hong, H. Chen, Q. Shi, J. Wang, X. Lu, N. Zhou, *Chem. Mater.* **2020**, *32*, 8868.
- [32] J. Fischer, M. Wegener, *Laser Photonics Rev.* **2013**, *7*, 22.
- [33] C. N. LaFratta, J. T. Fourkas, T. Baldacchini, R. A. Farrer, *Angew. Chem., Int. Ed.* **2007**, *46*, 6238.
- [34] J. T. Fourkas, in *Three-Dimensional Microfabrication Using Two-Photon Polymerization* (Ed: T. Baldacchini), William Andrew Publishing, Oxford, UK **2020**, pp. 57–76.
- [35] B. H. Cumpston, S. P. Ananthavel, S. Barlow, D. L. Dyer, J. E. Ehrlich, L. L. Erskine, A. A. Heikal, S. M. Kuebler, I. Y. S. Lee, D. McCord-Maughon, J. Qin, H. Röckel, M. Rumi, X. L. Wu, S. R. Marder, J. W. Perry, *Nature* **1999**, *398*, 51.
- [36] C. M. Spadaccini, in *Micro Nano Technologies* (Ed: C. M. Spadaccini), William Andrew Publishing, Oxford, UK **2020**, pp. 671–681.
- [37] F. Mayer, S. Richter, J. Westhauser, E. Blasco, C. Barner-Kowollik, M. Wegener, *Sci. Adv.* **2019**, *5*, eaau9160.
- [38] D. Jang, L. R. Meza, F. Greer, J. R. Greer, *Nat. Mater.* **2013**, *12*, 893.
- [39] A. Vyatskikh, S. Delalande, A. Kudo, X. Zhang, C. M. Portela, J. R. Greer, *Nat. Commun.* **2018**, *9*, 593.
- [40] J. K. Hohmann, G. Von Freymann, *Adv. Funct. Mater.* **2014**, *24*, 6573.
- [41] A. Frölich, J. Fischer, T. Zebrowski, K. Busch, M. Wegener, *Adv. Mater.* **2013**, *25*, 3588.
- [42] M. A. Zeeshan, R. Grisch, E. Pellicer, K. M. Sivaraman, K. E. Peyer, J. Sort, B. Özkale, M. S. Sakar, B. J. Nelson, S. Pané, *Small* **2014**, *10*, 1284.
- [43] R. A. Farrer, C. N. LaFratta, L. Li, J. Praino, M. J. Naughton, B. E. A. Saleh, M. C. Teich, J. T. Fourkas, *J. Am. Chem. Soc.* **2006**, *128*, 1796.
- [44] A. Radke, T. Gissibl, T. Klotzbücher, P. V. Braun, H. Giessen, *Adv. Mater.* **2011**, *23*, 3018.
- [45] J. Bauer, S. Hengsbach, I. Tesari, R. Schwaiger, O. Kraft, *Proc. Natl. Acad. Sci. USA* **2014**, *111*, 2453.
- [46] N. Muller, J. Haberko, C. Marichy, F. Scheffold, *Adv. Opt. Mater.* **2014**, *2*, 115.
- [47] L. R. Meza, S. Das, J. R. Greer, *Science* **2014**, *345*, 1322.
- [48] H. Xia, J. Wang, Y. Tian, Q. D. Chen, X. B. Du, Y. L. Zhang, Y. He, H. B. Sun, *Adv. Mater.* **2010**, *22*, 3204.
- [49] *Multiphoton Lithography: Techniques, Materials and Applications* (Eds: J. Stampfl, R. Liska, A. Ovsianikov), Wiley-VCH, Weinheim, Germany **2016**.
- [50] J. Z. Manapat, Q. Chen, P. Ye, R. C. Advincula, *Macromol. Mater. Eng.* **2017**, *302*, 1600553.
- [51] M. Layani, X. Wang, S. Magdassi, *Adv. Mater.* **2018**, *30*, 1706344.
- [52] A. Vyatskikh, R. C. Ng, B. Edwards, R. Julia, A. Vyatskikh, R. C. Ng, B. Edwards, J. R. Greer, *Proc. SPIE* **2019**, *10930*, 109300H.
- [53] J. W. Halloran, *Annu. Rev. Mater. Res.* **2016**, *46*, 19.
- [54] T. Ikegami, M. P. Stocker, K. Monaco, J. T. Fourkas, S. Maruo, *Jpn. J. Appl. Phys.* **2012**, *51*, 06FL17.
- [55] D. W. Yee, M. L. Lifson, B. W. Edwards, J. R. Greer, *Adv. Mater.* **2019**, *31*, 1901345.
- [56] Q. Wen, Z. Yu, R. Riedel, *Prog. Mater. Sci.* **2020**, *109*, 100623.
- [57] S. Park, D. H. Lee, H. I. Ryoo, T. W. Lim, D. Y. Yang, D. P. Kim, *Chem. Commun.* **2009**, 4880.
- [58] L. Brigo, J. E. M. Schmidt, A. Gandin, N. Michieli, P. Colombo, G. Brusatin, *Adv. Sci.* **2018**, *5*, 1800937.
- [59] D. Gailevičius, V. Padolskytė, L. Mikoliūnaitė, S. Šakirzanovas, S. Juodkakis, M. Malinauskas, *Nanoscale Horiz.* **2019**, *4*, 647.
- [60] M. Malinauskas, S. Sakirzanovas, V. Padolskytė, D. Gailevičius, V. Mizeikis, K. Staliunas, S. Juodkakis, L. Jonusauskas, L. Mikoliūnaitė, T. Katkus, R. Gadonas, *Proc. SPIE* **2018**, *10675*, 106750U.
- [61] L. Guo, H. Xia, H. Fan, Y. Zhang, Q. Chen, *Opt. Lett.* **2010**, *35*, 1695.
- [62] A. Vyatskikh, R. C. Ng, B. Edwards, R. M. Briggs, J. R. Greer, *Nano Lett.* **2020**, *20*, 3513.
- [63] C. Yeh, H. Zan, O. Soppera, *Adv. Mater.* **2018**, *30*, 1800923.
- [64] X. Zhang, X. Wu, J. Shi, *J. Mater. Res. Technol.* **2020**, *9*, 9029.
- [65] B. Buchegger, J. Kreutzer, B. Plochberger, R. Wollhofen, D. Sivun, J. Jacak, G. J. Schütz, U. Schubert, T. A. Klar, *ACS Nano* **2016**, *10*, 1954.
- [66] Q. Hu, X. Z. Sun, C. D. J. Parmenter, M. W. Fay, E. F. Smith, G. A. Rance, Y. He, F. Zhang, Y. Liu, D. Irvine, C. Tuck, R. Hague, R. Wildman, *Sci. Rep.* **2017**, *7*, 17150.
- [67] J. C. Watts, P. A. Larson, in *Kirk-Othmer Encyclopedia of Chemical Technology*, Wiley, New York **2002**.
- [68] J. I. Goldstein, D. E. Newbury, P. Echlin, D. C. Joy, C. E. Lyman, E. Lifshin, L. Sawyer, J. R. Michael, *Scanning Electron Microscopy and X-Ray Microanalysis*, Springer, Boston, MA **2003**, p. 271.
- [69] D. Lafatzis, K. Mergia, *J. Appl. Phys.* **2013**, *114*, 144308.
- [70] Y. Zhao, W. Li, M. Zhang, K. Tao, *Catal. Commun.* **2002**, *3*, 239.
- [71] C. Ciszak, M. Mermoux, G. Gutierrez, F. Leprêtre, C. Duriez, I. Popa, L. Fayette, S. Chevalier, *J. Raman Spectrosc.* **2019**, *50*, 425.
- [72] G. Pezzotti, A. A. Porporati, *J. Biomed. Opt.* **2004**, *9*, 372.
- [73] X. Zhao, D. Vanderbilt, *Phys. Rev. B* **2002**, *65*, 075105.

- [74] H. Richter, Z. P. Wang, L. Ley, *Solid State Commun.* **1981**, *39*, 625.
- [75] V. V. Rodaev, S. S. Razlivalova, A. O. Zhigachev, V. M. Vasyukov, Y. I. Golovin, *Polymers* **2019**, *11*, 1067.
- [76] S. N. Basahel, T. T. Ali, M. Mokhtar, K. Narasimharao, *Nanoscale Res. Lett.* **2015**, *10*, 73.
- [77] J. Málek, L. Beneš, T. Mitsuhashi, *Powder Diffr.* **1997**, *12*, 96.
- [78] C. J. Howard, R. J. Hill, B. E. Reichert, *Acta Crystallogr., Sect. B* **1988**, *44*, 116.
- [79] C. Lin, C. Zhang, J. Lin, *J. Phys. Chem. C* **2007**, *111*, 3300.
- [80] C. Urlacher, J. Mugnier, *J. Raman Spectrosc.* **1996**, *27*, 785.
- [81] O. Saligheh, R. Khajavi, M. E. Yazdanshenas, A. Rashidi, *J. Macromol. Sci., Part B: Phys.* **2016**, *55*, 605.
- [82] A. Mondal, A. Zachariah, P. Nayak, B. B. Nayak, *J. Am. Ceram. Soc.* **2010**, *93*, 387.
- [83] Y. Cong, B. Li, S. Yue, D. Fan, X. J. Wang, *J. Phys. Chem. C* **2009**, *113*, 13974.
- [84] Z. Wang, B. Yang, Z. Fu, W. Dong, Y. Yang, W. Liu, *Appl. Phys. A: Mater. Sci. Process.* **2005**, *81*, 691.
- [85] S. Ashraf, M. Irfan, D. Kim, J. H. Jang, W. T. Han, Y. D. Jho, *Ceram. Int.* **2014**, *40*, 8513.
- [86] C. Zhang, C. Li, J. Yang, Z. Cheng, Z. Hou, Y. Fan, J. Lin, *Langmuir* **2009**, *25*, 7078.
- [87] B. Henderson, *Contemp. Phys.* **2002**, *43*, 273.
- [88] C. F. Klingshirm, *Semiconductor Optics*, Springer-Verlag, Berlin, Germany **2012**.
- [89] W. B. Fowler, *Phys. Rev.* **1964**, *135*, A1725.
- [90] F. Karsai, P. Tiwald, R. Laskowski, F. Tran, D. Koller, S. Gräfe, J. Burgdörfer, L. Wirtz, P. Blaha, *Phys. Rev. B* **2014**, *89*, 125429.
- [91] S. Kumar, A. K. Ojha, *J. Alloys Compd.* **2015**, *644*, 654.
- [92] K. Smits, L. Grigorjeva, D. Millers, A. Sarakovskis, A. Opalinska, J. D. Fidelus, W. Lojkowski, *Opt. Mater.* **2010**, *32*, 827.
- [93] D. Nishida, M. Kusaba, T. Yatsuhashi, N. Nakashima, *Chem. Phys. Lett.* **2008**, *465*, 238.
- [94] C. Y. M. Kusaba, N. Nakashima, W. Kawamura, Y. Izawa, *J. Alloys Compd.* **1993**, *192*, 284.
- [95] H. Li, Y. Wang, *Inorg. Chem.* **2017**, *56*, 10396.
- [96] A. Biswas, C. S. Friend, P. N. Prasad, *Mater. Lett.* **1999**, *39*, 227.
- [97] J. Andres, R. D. Hersch, J. E. Moser, A. S. Chauvin, *Adv. Funct. Mater.* **2014**, *24*, 5029.
- [98] Y. C. Lin, M. Bettinelli, M. Karlsson, *Chem. Mater.* **2019**, *31*, 3851.
- [99] J. Qiao, J. Zhao, Q. Liu, Z. Xia, *J. Rare Earths* **2019**, *37*, 565.
- [100] F. Steudel, T. Lisec, P. W. Nolte, U. Hofmann, T. von Wantoch, F. Lofink, S. Schweizer, *Opt. Express* **2019**, *27*, 9097.
- [101] H. Gao, G. F. R. Chen, P. Xing, J. W. Choi, H. Y. Low, D. T. H. Tan, *Adv. Opt. Mater.* **2020**, *8*, 2000613.
- [102] F. Frascella, G. González, P. Bosch, A. Angelini, A. Chiappone, M. Sangermano, C. F. Pirri, I. Roppolo, *ACS Appl. Mater. Interfaces* **2018**, *10*, 39319.
- [103] G. Santomauro, M. Stiefel, L. P. H. Jeurgens, J. Bill, *Adv. Biosyst.* **2020**, *4*, 1900301.
- [104] G. Kräuter, A. Eberhardt, F. Peskoller, N. S. Güldal, A. Lell, R. Ritasalo, T. Pilvi, M. Römer, G. Domann, P. Löbmann, *J. Sol-Gel Sci. Technol.* **2021**, *97*, 458.
- [105] S. Hu, Y. Liu, Y. Zhang, Z. Xue, Z. Wang, G. Zhou, C. Lu, H. Li, S. Wang, *J. Eur. Ceram. Soc.* **2019**, *39*, 2731.
- [106] Q. Yao, P. Hu, P. Sun, M. Liu, R. Dong, K. Chao, Y. Liu, J. Jiang, H. Jiang, *Adv. Mater.* **2020**, *32*, 1907888.
- [107] J. Wang, W. Yin, X. He, Q. Wang, M. Guo, S. Chen, *Sci. Rep.* **2016**, *6*, 35020.
- [108] K. Soga, K. Tokuzen, K. Tsuji, T. Yamano, N. Venkatachalam, H. Hyodo, H. Kishimoto, *Proc. SPIE* **2010**, *7598*, 759807.
- [109] B. P. Bratton, J. W. Shaevitz, T. Abraham, *PLoS One* **2015**, *10*, e0134616.